Macromolecules

pubs.acs.org/Macromolecules Article

# Conflicting Effects of Extreme Nanoconfinement on the Translational and Segmental Motion of Entangled Polymers

R. Bharath Venkatesh and Daeyeon Lee*

Cite This: *Macromolecules* 2022, 55, 4492−4501 Read Online

ACCESS | Metrics & More | Article Recommendations | Supporting Information

**ABSTRACT:** Physically confining polymers into nanoscale pores induces significant changes in their dynamics. Although different results on the effect of confinement on the dynamics of polymers have been reported, changes in the segmental mobility of polymers typically are correlated with changes in their chain mobility due to increased monomeric relaxation times. In this study, we show that translational and segmental dynamics of polymers confined in disordered packings of nanoparticles (NPs) can exhibit completely opposite behavior. We monitor the capillary rise dynamics of entangled polystyrene (PS) in disordered packings of silica NPs of 7 and 27 nm diameter. The effective viscosity of PS in 27 nm $SiO_2$ NP packings, inferred based on the Lucas−Washburn equation, is significantly smaller than the bulk viscosity, and the extent of reduction in the translational motion due to confinement increases with the molecular weight of PS, reaching 4 orders of magnitude reduction for PS with a molecular weight of 4M g/mol. The glass transition temperature of entangled PS in the packings of 27 nm $SiO_2$ NPs, however, increases by 45 K, indicating significant slowdown of segmental motion. Interestingly, confinement of the polymers into packings made of 7 nm $SiO_2$ NPs results in molecular weight-independent effective viscosity. The segmental dynamics of PS in 7 nm $SiO_2$ NP packings are slowed down even further, as evidenced by a 65 K increase in glass transition temperature. These seemingly disparate effects are explained by the microscopic reptation-like transport controlling the translational motion and the physical confinement affecting the segmental dynamics under extreme nanoconfinement. Although we do not fully understand the origin of the molecular weight-independent effective viscosity of PS in the 7 nm $SiO_2$ NP packings, nonlinear flow and hyperconfinement effects may be playing a role. The novel flow behavior that we observe opens new ground for further theoretical exploration of the dynamics of extremely confined polymer melts.

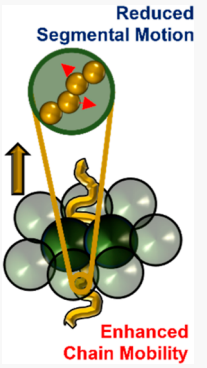


## INTRODUCTION

Infiltration of a polymer into nanoscale pores bears significant importance for a number of processes and phenomena.[1−10] Capillary rise of a polymer into anodized aluminum oxide (AAO) membranes has been used to prepare polymer nanowires and nanotubes.[11−13] For example, the Rayleigh instability of polymeric fluids inside AAO pores has been used to template nanorods with unique curvature.[14,15] Nanoporous templates made from poly-(*N*-isopropyl) acrylamide have been filled with poly(dimethylsiloxane) and then crosslinked to obtain composites of hydrophobic and hydrophilic materials.[16] Capillary rise infiltration (CaRI) of polymers into the interstitial pores of nanoparticle (NP) packings[2,3,5,17−20] has emerged as a powerful approach to prepare nanocomposite films and membranes with extremely high volume fractions of nanomaterials. Such polymer-infiltrated NP films have superb fracture toughness, thermal stability, and corrosion resistance.[3,17,21,22] In addition to material fabrication, infiltration of high-molecular-weight (MW) polymers into nanopores is an important step in enabling upcycling of polymers through heterogeneous catalysis.[23]

In many instances, polymer chains undergoing capillary rise into nanoporous media are subjected to extreme nanoconfinement as chains are confined to pores that are substantially smaller than their unperturbed chain dimensions. Such nanoconfinement can bring about significant changes to the ability of the polymer chains to undergo translational and segmental motion. For example, studies on the motion of unentangled polystyrene (PS) into silica ($SiO_2$) NP packings reported an increase in the effective viscosity and the glass transition temperature ($T_g$) of the polymer with an increase in the extent of confinement.[24,25] Confinement slows down the polymer at the chain level, leading to an increase in the effective viscosity by 2 orders of magnitude for the most heavily confined unentangled polymers. Contrary to reports of slowdown in unentangled polymers under confinement, a decrease in the viscosity of confined polymers has been reported for the capillary rise of high-MW PS and poly-(ethylene oxide) (PEO) into the nanopores of AAO membranes,[26−28] as well as in the diffusion studies of entangled polymers in cylindrical pores.[29−31] The $T_g$ of PEO decreased by 6 K in 65 nm diameter AAO nanopores

Received: January 20, 2022
Revised: April 8, 2022
Published: May 24, 2022

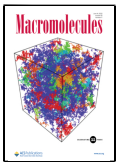







https://doi.org/10.1021/acs.macromol.2c00145
*Macromolecules* 2022, 55, 4492−4501

compared to that of the bulk PEO, whereas the $T_g$ of PS undergoing capillary rise in AAO nanopores showed little change compared to the bulk values.[26,27] The segmental dynamics of unentangled PS and poly(2-vinyl pyridine) (P2VP) in the CaRI films of $SiO_2$ were found to be significantly reduced due to geometric confinement.[32] In packings of 7 nm $SiO_2$ NPs, for example, the $T_g$ of unentangled PS increases by 32 K, indicating huge levels of segmental slowdown arising from nanoconfinement. These results show that the exact nature of changes in the translational and segmental motion of polymer chains depends on the geometry and the extent of confinement. In general, however, the changes in the translational dynamics of polymers are consistent with those observed in segmental motion in the corresponding systems. Indeed, polymer dynamics at different length scales are known to be correlated; that is, a reduction in segmental mobility typically corresponds to reduction in chain mobility due to increased monomeric relaxation times.[33−35] To our knowledge, very few reports have shown the opposite trend—slowdown of segmental dynamics, for example, accompanied by speed-up of chain motion.

In this study, we investigate the effect of extreme nanoconfinement imposed by disordered packings of $SiO_2$ NPs on the capillary rise dynamics and segmental motion of high-MW PS. We track infiltration dynamics of high-MW PS into disordered $SiO_2$ NP packings using in situ ellipsometry and extract the effective viscosity of the confined polymers using the Lucas−Washburn equation. We also measure the $T_g$ of PS under confinement using ellipsometry by measuring refractive index changes with temperature on a controlled cooling ramp. Our results show that the confinement can have conflicting effects on the imbibition dynamics and segmental motion of the polymers; while the capillary rise dynamics of the polymer is enhanced in 27 nm $SiO_2$ NP packings, their segmental motion dynamics is reduced. Despite the segmental slowdown, the chains show faster than bulk motion with almost 4 orders of magnitude reduction in the effective viscosity for the longest chains (PS 4M with unperturbed $R_g \sim$ 50 nm) in the 27 nm NP packings. In 7 nm $SiO_2$ NP packings, translational motion shows little dependence on their MW, while their segmental motion is substantially slowed down. These conflicting effects are reconciled by considering the different length scale and timescales of these motions and the effects controlling them. We discuss the possible reasons behind these findings, which could potentially provide important guidance on the fabrication and applications of highly loaded films and membranes prepared *via* CaRI.

## EXPERIMENTAL METHODS

**Materials.** PS of different MWs ($M_n$),173,000 g/mol (173k), polydispersity index (PDI) = 1.06; 498,000 g/mol (498k), PDI = 1.08; 1,000,000 g/mol (1M), PDI = 1.05; 2,100,000 g/mol (2.1M), PDI = 1.15; and 4,049,000 g/mol (4M), PDI = 1.09, are purchased from Polymer Source Inc. Aqueous suspensions of silica ($SiO_2$) NPs with average diameters of 7 nm (Ludox SM-30, 30 wt % suspension in water) and 27 nm (Ludox TM-50, 50 wt % suspension in water) are purchased from Sigma-Aldrich. Silicon wafers (10 cm diameter, 0.5 mm thickness, 0−100 Ω·cm resistivity) are procured from University Wafer.

**Preparation and Characterization of Polymer−NP Bilayer Films.** Silicon wafers are cut into approximately 1 cm × 1 cm squares. The wafers are rinsed with acetone, isopropanol, and deionized water and dried under nitrogen. Subsequently, the wafers are treated with oxygen plasma treatment for 4 min. The $SiO_2$ NP suspension is diluted to 10−15 wt % with water. The NP solutions are bath-sonicated for at least 4 h and filtered using a 0.45 $\mu$m hydrophilic syringe filter purchased from Fisher Scientific. The solutions are spin-coated on top of the cleaned silicon wafers at 2200−2500 rpm for 1.5 min to get NP packings of 250−300 nm thickness.

To prepare PS films, 2−2.5 wt % PS solution is prepared by dissolving PS in toluene and then sonicated and filtered using a 0.20 $\mu$m hydrophobic PTFE syringe filter purchased from Sigma-Aldrich. 200−250 nm-thick PS layers are prepared by spin-coating the PS solution at 2000 rpm for 90 s onto cleaned silicon wafers using a WS-400BZ-6NPP/Lite spin-coater from Laurell Technologies Corporation. The polymer film is cut at the edges using a razor blade without damaging the substrate. The film is then immersed slowly into a water bath at an angle of 45° to the water surface such that the PS film delaminates from the substrate and floats on the water surface. The entangled nature of the PS film enables delamination from the substrate. NP film, spin-coated earlier on the silicon substrate, is then immersed in a water bath to capture the free-standing polymer film on top of the NP packing to get a polymer−NP bilayer. The bilayer is dried overnight.

Scanning electron microscopy (SEM) images of the cross-section of the samples are taken using a JEOL 7500F HRSEM. Cross-sectional images are taken by cleaving the sample using a diamond scribe and mounting the sample vertically on a stub with the cross-section facing the electron beam. The samples are sputtered with a 4 nm iridium layer using a Quorom plasma generating sputter coater prior to imaging to prevent charging. An accelerating voltage of 5 kV and an emission current of 20 $\mu$A at a working distance of ∼8 mm are used to image the samples.

**Characterization of the Polymer CaRI Process.** Polymer infiltration into the voids of the NP packing is monitored in situ using a J.A. Woollam Alpha-SE spectroscopic ellipsometer. A bilayer sample is annealed above the glass transition temperature ($T_g$) of the polymer using a Linkam THMS350 V heating stage mounted on the ellipsometer. A temperature ramp is specified using the Linksys software, which increases the temperature of the heating stage at a rate of 30 °C/min to the desired set point temperatures (155, 160, and 165 °C) and holds it for a specified time (10−12 h) at the set-point temperature. The sample is adhered to the heating stage using a thermal paste Arctic Silver Ceramic polysynthetic thermal compound which allows good contact without thermal insulation. To prevent heat loss due to exposure to the atmosphere, the setup is covered using a thermocol ice box purchased from Amazon. Annealing is stopped when the dynamic data stops changing, which takes typically 3−12 h depending on the MW and temperature.

The ellipsometry data are collected in the wavelength ($\lambda$) range of 380−900 nm at an incident angle of 70°. The CompleteEASE software package provided by J.A. Woollam uses a model-based approach for the fitting of the amplitude change ($\psi$) and phase change ($\Delta$) of the polarized light to a three-layer Cauchy model (NP packing, composite, and polymer) on a silicon substrate with a native oxide layer. The Cauchy model for each layer is expressed as $n(\lambda) = A + B/\lambda^2 + C/\lambda^4$ and $k(\lambda) = 0$, where $A$, $B$, and $C$ are the optical constants, $\lambda$ is the wavelength (in $\mu$m), and $n$ and $k$ are the index of refraction and extinction coefficient, respectively. The fitting procedure allows extraction of physical parameters—the thickness and refractive index of each layer of the sample.

**Glass Transition Temperature ($T_g$) Measurements.** The glass transition temperature ($T_g$) of the residual polymer and the polymer confined in the NP packing is measured using a J.A. Woollam M-2000V spectroscopic ellipsometer. The postinfiltration sample, that is, the polymer-infiltrated film with a residual polymer layer on top, is mounted onto a Linkam THMS 600 temperature-controlled stage attached to the ellipsometer. The in situ ellipsometry sampling rate is 1 s, and three heating and cooling cycles between 30 and 200 °C are performed for each sample, with a heating rate of 30 K/min and a cooling rate of 10 K/min. The sample is heated at 30 K/min to the target temperature of 200 °C and then annealed at the same temperature for 2 min; subsequently, it is cooled at 10 K/min to 20 °C and held there for 5 min before repeating the entire process again.


https://doi.org/10.1021/acs.macromol.2c00145
Macromolecules 2022, 55, 4492−4501

The objective of the heating step is to take the sample to a high temperature ($T$ = bulk $T_g$ + 100 °C) and anneal it at high temperature to ensure that all thermal history of the sample is erased before beginning the cooling at a controlled rate of 10 K/min. The $T_g$ is measured during the cooling cycle, which would not depend on the thermal history of the material. The thickness and refractive index of the residual polymer film and the composite are determined by fitting the cooling ramp raw data to the Cauchy model. The $T_g$ of the confined polymer for the composite is determined *via* the intersection of the linear fits to the melt and glassy regimes in the plots of nanocomposite refractive index versus temperature. $T_g$ of nonconfined PS is determined using the same protocol on the residual polymer layer's thickness versus temperature plot (see the Supporting Information for details). The change in the thickness of the overlying film with temperature is governed by polymer bulk dynamics, and the change in the refractive index of the composite is governed by the confined polymer dynamics. Measurement of both quantities on a controlled temperature ramp allows us to determine the temperature at which the slope of each quantity changes—these points mark the glass transition temperatures of the bulk and the confined polymer. Samples had at least 100 nm-thick residual polymer layers on top such that the measured $T_g$ in the thin films would be close to the bulk value.

## RESULTS AND DISCUSSION

We take advantage of the high surface energy of $SiO_2$ NPs and the high curvature of the nanopores in the NP packing to induce CaRI of high-MW entangled PS into the pores of the NP packings. Infiltration proceeds predominantly by the action of surface tension as the capillary forces are dominant over gravity in the nanovoids. A bilayer of PS and $SiO_2$ NP packing is prepared by first spin-coating $SiO_2$ NPs onto a silicon (Si) wafer and subsequently depositing a free-standing film of PS atop the NP layer. The SEM image of the bilayer before annealing as seen in Figure 1a shows the randomly distributed,

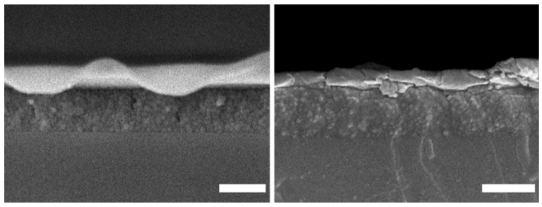

**Figure 1.** (a) SEM image of the PS-$SiO_2$ bilayer before annealing: the polymer (PS—173k g/mol) film is atop a 250 nm NP packing made from 27 nm-diameter $SiO_2$ NPs and (b) SEM image of a bilayer annealed at 165 °C with the composite CaRI film at the bottom and the residual polymer layer on top. The composite layer shows the pores between the particles filled with polymers. Scale bars represent 250 nm.

interconnected, nanometer-sized pores in the NP packing with the PS layer on top of the packing. Heating this bilayer above the glass transition temperature ($T_g$) of PS (~100 °C) leads to the imbibition of PS into the pores of the packing *via* capillarity. The infiltration process is monitored by spectroscopic ellipsometry, which allows us to measure the dynamics of the capillary rise of polymers into the packing. PS infiltrates the NP packing uniformly without creating any cracks. A residual PS layer on top of the PS–NP composite layer can be clearly observed, as shown in Figure 1b. Such a sample is subsequently used to characterize the $T_g$ of the confined PS and the unconfined PS in the residual layer.

Prior to the infiltration of PS into the NP packing, the thicknesses of the NP packing and PS layer are determined by fitting the ellipsometry data to a two-layer Cauchy model. The refractive index of the PS layer matches that of a neat PS film. The refractive index for the NP packing is used along with the bulk values of $SiO_2$ and air to infer the porosity of the packing (~34%). Upon heating, PS invades the NP packing with a uniform front, which we track using a three-layer Cauchy model composed of a neat polymer layer on top, a composite layer in the middle, and an unfilled NP packing at the bottom. A sharp invading front between the composite and the unfilled NP packing can be detected based on modeling of the ellipsometry data. The thickness of the composite layer gives the height of the infiltrating front with time. PS infiltrates the NP packing more rapidly at higher temperatures, as shown in Figure 2a. For each curve plotted in the inset of Figure 2a, a linear region can be clearly seen in the middle section of the time range. The linear region of infiltration trajectory is used to extract the slope to calculate the viscosity.

To quantify the dynamics of CaRI, the effective viscosity of PS infiltrating the NP packing is inferred based on the Lucas–Washburn equation[36,37]

$$h^2 = \left(\frac{\gamma R_{pore} \cos\theta}{4\eta_{conf}\tau^2}\right)t \quad (1)$$

where $\gamma$ is the surface tension of the polymer, $R_{pore}$ is the pore radius, $\theta$ is the equilibrium contact angle at the triple line between the surface of the pore (silica NP), air, and the polymer, $\eta_{conf}$ is the effective viscosity of the polymer melt undergoing capillary rise, and $\tau$ is the tortuosity of the packing. Although the NP packings provide a tortuous path of nanopores with varying pore sizes, dynamics of capillary rise into such porous media has been used to estimate the rheological properties of a variety of simple and complex fluids.[38−46] The average pore size in a random close packing of spheres has been reported to be ~30% of the radius of the particle, which we use for $R_{pore}$.[47] The tortuosity of the packing is reported to be 1.95 for interconnected pores in a packing made of randomly close-packed spheres.[48] The surface tension of PS is taken from the bulk values from the literature, and the contact angle of PS on $SiO_2$ is taken as 20°.[49] The effective viscosity of the confined PS ($\eta_{conf}$) can be calculated based on these values by plotting the infiltration kinetics data as $h^2$ versus $t$ and extracting the slope. The calculated viscosity is the effective viscosity under confinement, and it is compared with the bulk viscosity ($\eta_0$) of PS from the published data (see the Supporting Information for more details).[50−52] Pinning of rising fluid into nanopores is possible; however, if pinning of the moving front were to exist, the effective viscosity we calculate based on eq 1 would provide a conservative estimate of the viscosity of the confined polymer.

The confined viscosity of PS in 27 nm $SiO_2$ NP packing and the bulk viscosity of PS are plotted for three different temperatures, as shown in Figure 2b. The confined viscosity is lower than the bulk viscosity in all cases except for PS-173k, for which the two values are very similar. The difference between the confined and bulk viscosity values increases with MW, and the effective viscosity under confinement is 4 orders of magnitude lower than the bulk viscosity at MW = 4M g/mol. The effect of MW on the confined viscosity is less significant than that on the bulk viscosity, which follows the bulk reptation predictions ($\eta \sim MW^{3.4}$). This deviation from the bulk exponent signals that the flow mechanism is different from bulk reptation. A novel flow mechanism has been


https://doi.org/10.1021/acs.macromol.2c00145
Macromolecules 2022, 55, 4492−4501

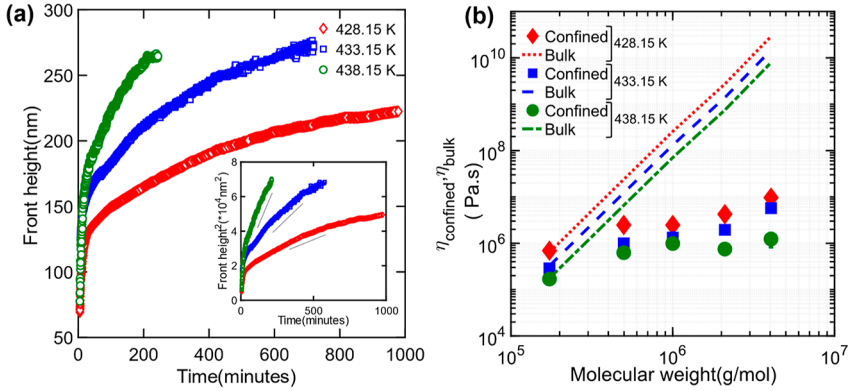


**Figure 2.** (a) Front height for PS-4M g/mol infiltrating into $SiO_2$ (27 nm) NP packings is plotted against the time (in minutes) at three different temperatures—155 (diamonds), 160 (squares), and 165 (circles) °C. The inset shows the Lucas−Washburn scaling of the dynamic data when plotted as $h^2$ vs $t$. The dashed lines parallel to the main curves are indicative of the slope of the curves used to calculate viscosity from the dynamic data. (b) Confined viscosity of high-MW PS (173k to 4M g/mol) infiltrating $SiO_2$ (27 nm) NP packings measured using ellipsometric tracking at three different temperatures—155 (diamonds), 160 (squares), and 165 (circles) °C. The dashed lines show the bulk viscosity calculated using published predictions (see the Supporting Information for details) for zero shear viscosity of entangled PS.[50−52]

proposed to explain the motion of confined entangled chains,[53] which will be discussed in detail later.

The effective viscosity of PS confined in packings of 7 nm $SiO_2$ NPs shows a unique trend quite different from the effective viscosity of PS in 27 nm $SiO_2$ NP packings. As can be seen in Figure 3, the effective viscosity stays largely unaffected

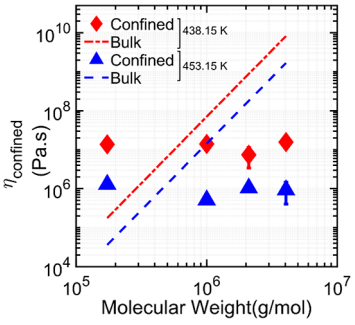


**Figure 3.** Confined viscosity of high-MW PS (173k to 4M g/mol) infiltrating into $SiO_2$ (7 nm) NP packings measured using ellipsometric front tracking at two different temperatures—165 °C (diamonds) and 180 °C (triangles). The dashed lines show the bulk viscosity calculated using published predictions (see the Supporting Information for details) for zero shear viscosity of entangled PS.[50−52]

across a large range of MW and depends only on the temperature. While the PS-4M shows enhanced translational mobility under confinement compared to the bulk PS, PS-173k has effective confined viscosity that is higher than that of bulk PS. Such an observation, to our best knowledge, has not been previously reported, and we offer our hypotheses responsible for this trend later.

To check if the enhanced translational mobility of the confined polymers is affected by changes in the segmental motion, the $T_g$ values of confined PS in both 7 and 27 nm packings are measured and compared to the bulk $T_g$ measured using the residual polymer film atop the composite layer (see the Supporting Information for details). Surprisingly, there is a slowdown in segmental motion, as seen from the increase in the confined $T_g$ relative to the bulk $T_g$ as shown in Figure 4. The bulk $T_g$ values are close to the previously reported $T_g$ for bulk PS (100−103 °C). In contrast, $T_g$ of PS confined in $SiO_2$

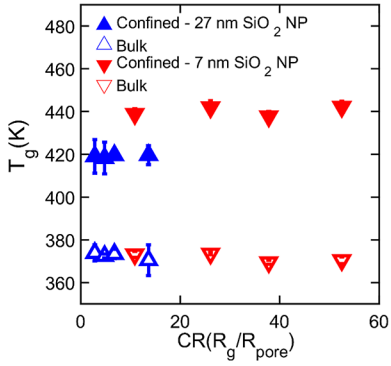


**Figure 4.** Glass transition temperatures ($T_g$) for confined and bulk high-MW PS at different CRs in 27 nm (triangle) and 7 nm (inverted triangle) $SiO_2$ NP packings. The closed symbols are $T_g$ measurements done for the polymer confined within the NP packings after infiltration and the open symbols are for polymers in the thin residual film (>100 nm) left atop the NP packing after infiltration. The latter measurements reflect the bulk $T_g$ values of entangled Polystyrene.

nanopores is about 45 K higher than the bulk PS $T_g$ and does not change much with MW. For PS confined in the pores of 7 nm $SiO_2$ NPs, the difference between the confined and the bulk $T_g$ is even larger (around 65 K) and does not depend strongly on the MW. These observations are consistent with recent reports that showed that PS confined in the $SiO_2$ NP packings has significantly higher $T_g$ compared to bulk[25,32] and more importantly suggest that the translational motion of high-MW PS in the $SiO_2$ NP packings is not closely coupled to their segmental motion.

Polymers are subjected to extremely high degrees of confinement in the pores (size: 1−4 nm) of NP packings. For example, by varying the MW of PS between 173,000 g/mol (PS-173k) and 4,000,000 g/mol (PS-4M) and using either 27 nm or 7 nm $SiO_2$ NPs, the extent of confinement, defined by the ratio of the radius of gyration of polymer and the average pore size, can be varied between 2 and 60. Thus, at the highest level of confinement, the chain dimension can be an order of magnitude higher than the confining pore dimension. The effect of such extreme nanoconfinement is complex, as discussed here.


https://doi.org/10.1021/acs.macromol.2c00145
Macromolecules 2022, 55, 4492−4501

**Enhanced Translational Mobility in 27 nm Silica NP Packings.** To assess how the extent of confinement affects the dynamics of confined PS in the $SiO_2$ NP packings, the effective viscosity of PS confined in 27 nm $SiO_2$ NP packings is normalized with respect to the bulk viscosity and plotted as a function of the confinement ratio (CR), which is defined as the ratio of the radius of gyration of PS and the average pore size ($R_g/R_{pore}$). The reduction in the effective viscosity with increasing confinement is clearly seen in Figure 5 with a

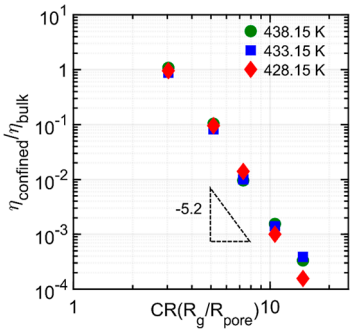


**Figure 5.** Confined viscosity of high-MW PS (173k to 4M g/mol) infiltrating $SiO_2$ (27 nm) NP packings is normalized with the bulk viscosity at three different temperatures—155 (diamonds), 160 (squares), and 165 (circles) °C—and plotted against the CR. The scaling is extracted from the slope of the best linear fit of the data points.

temperature-independent scaling of the normalized viscosity with the CR. Remarkably, at the highest level of confinement (PS-4M, CR ∼ 15), the effective viscosity falls by almost 4 orders of magnitude with respect to the bulk. Note that the viscosity is normalized with respect to the bulk viscosity at the same temperature and not at a fixed distance from $T_g$. The magnitude of the relative viscosity change is even greater if we take the latter approach, but the scaling with the CR remains the same (see the Supporting Information for scaling with a fixed distance from $T_g$).

We consider some possible reasons behind the observed reduction in the effective viscosity of PS in 27 nm $SiO_2$ NP packings. MD simulations have shown that dynamic contact angle correction is necessary to use the Lucas−Washburn equation to model the flow of non-Newtonian fluids such as polymer melts in micro- and nanochannels.[54−56] The measured viscosity, however, has been found to be not sensitive to the dynamic contact angle in a prior study on the capillary rise of PEO (MW = 100 kg/mol to 1,000,000 g/mol) in the pores (pore diameters = 25 to 400 nm) of AAO membranes.[26] The marginal change in the viscosity by applying the dynamic contact angle correction could not explain the drastic reduction in the viscosity observed in their study. The magnitude of the calculated effective viscosity also is not sensitive to the choice of the contact angle (see the Supporting Information for the sensitivity analysis of calculated viscosity with contact angle). The trends with MW and confinement which are the main results of this study do not depend on the exact value of the contact angle of PS on $SiO_2$. Another possibility is that entangled polymers are known to undergo shear thinning due to chain disentanglement when they are subjected to high shear.[57] The local shear rate in the polymer during capillary rise in the NP packings, however, is not high enough to induce the drastic reduction in the effective viscosity that we observe (see the Supporting Information for details).

The enhancement in translational mobility that we observe in this work is similar to the reduction in the effective viscosity measured in prior reports on the capillary rise of PS and PEO in AAO.[26,27] A novel mechanism of fluid transport which involves plug flow of entangled polymeric melt in narrow capillaries with no-slip boundary conditions has been invoked to explain the reduction in viscosity.[58] In this mechanism, polymer chains reptate through an entangled mesh of constraints, which itself moves under the action of the external pressure gradient, provided by the capillary pressure.[53,58] A theoretical model developed for polymer flow in cylindrical nanopores considers two main effects in the capillary rise of polymers into capillaries:

(1) Slower-than-bulk rise of polymers at moderate confinement—this increased viscosity is postulated to come from the buildup of a dead zone of adsorbed polymers near the pore surface, which reduces the effective pore diameter which provides additional viscous resistance to polymer flow. This results in an increase in viscosity, which can be given by

$$\frac{\eta}{\eta_0} \sim \left(\frac{R_{eff}}{R}\right)^{-4} \tag{2}$$

where $R_{eff}$ is the reduced pore diameter due to the dead zone, $R$ is the original pore diameter, and the confined and bulk viscosities are given by $\eta_0$ and $\eta$.

(2) Faster-than-bulk rise of polymers at high confinement—this reduced viscosity arises from a reptation-like flow of polymers driven by the capillary pressure gradient in the NP packings. The expression for this is given by

$$\frac{\eta}{\eta_o} \sim \frac{NR^2}{\varphi\eta_o} \tag{3}$$

where $N$ is the number of Kuhn segments in the chain, $R$ is the pore radius, $\varphi$ is a constant that contains the bulk polymer properties including the entanglement length, and bulk viscosity is given by $\eta_0$. Combining the two terms gives

$$\frac{\eta}{\eta_o} = \left[\left(\frac{R_{eff}}{R}\right)^4 + \frac{\varphi\eta_o}{NR^2}\right]^{-1} \tag{4}$$

This equation can be used to describe the change in the effective viscosity of PS of any chain size in NP packings. We can apply eq 4 to our data in two ways: (a) keep $R$ constant and adjust N, which has been done for entangled PS confined in 27 nm $SiO_2$ NPs (Figure 5) and (b) keep $N$ constant and vary $R$, which is shown in Figure S4 in the Supporting Information, where the abscissa has been chosen to be $1/R$. Shown alongside are results from Yao et al.[53] We can see a remarkable similarity in the trends, although the theoretical prediction and the experimental results do not agree perfectly.

The first term on the right-hand side of eq 4 accounts for the reduction in chain mobility due to reduction of the pore radius from $R$ to $R_{eff}$ induced by the chains adsorbed on the wall; the second term represents microscopic reptation, where $\varphi$ accounts for the monomeric friction, entanglement length, and other constants. The first term dominates when $R_g \ll R$ in the case of underconfined polymers, whereas the microscopic reptation becomes important for confined polymers, where $R_g$


https://doi.org/10.1021/acs.macromol.2c00145
Macromolecules 2022, 55, 4492−4501

$\gg R$, such as the infiltration of entangled PS into nanopores of $SiO_2$ NP packings studied in our current work. If eq 4 is simplified by neglecting the first term as is valid for the case of extreme confinement in the nanopores used in this study, $\eta \sim N$, provided all other terms including the pore size are kept constant.

The normalized viscosity of confined PS in a 27 nm $SiO_2$ NP packing with respect to the CR shows $\frac{\eta}{\eta_o} \sim \left(\frac{R_g}{R_{pore}}\right)^{-5.2} \sim N^{-2.6}$. When combined with the scaling of zero-shear viscosity of entangled melts ($\eta_o \sim N^{3.4}$), the scaling for confined viscosity can be expressed as $\eta \sim N^{0.8}$, which is close to that expected from the model. This result is also close to the previously reported values of scaling exponents, 1.4 and 0.9 in studies on the capillary rise of PS and PEO into AAO nanopores, respectively.[26,27] The enhancement in mobility of confined PS in AAO nanopores has been explained with the help of disentanglement of chains and reduction in the density of confined chains. This leads to reduction in confined polymer viscosity and an expected scaling of flux with chain size as $N^{1.4}$.[27] The scaling is also similar to the entropic barrier model scaling proposed by Muthukumar[59] using a model developed for highly heterogeneous confinement in gels and concentrated solutions; however, entropic barriers to polymer diffusion cannot explain the enhanced chain dynamics seen here.

Recent work has highlighted the timescales involved in the adsorption of chains during and after imbibition into AAO nanopores.[60−62] Adsorption of chains to the NP surface can lead to arrested conformations of polymer chains on the surface of the NPs, leading to the dead zone. This dead zone of adsorbed chains increases flow viscosity by effectively decreasing the size of the pore.[53] In contrast, the reduction in the effective viscosity (i.e., faster-than-bulk motion) and its linear scaling with MW points to the reptation under capillary pressure gradient, playing a more important role than adsorption effects for entangled polymer flow. The reduced impact of adsorption could also be attributed to the slow kinetics of irreversible adsorption for longer chains, especially at high confinement.

**MW-Independent Viscosity in 7 nm Silica Packings.** High-MW polymers due to their high viscosity can exhibit slip at boundaries. When the slip length is high, there is very little radial variation in the velocity profile inside the pores. This constant-velocity plug flow due to high slip (where the slip length is so high that it wipes out any dependence of flow on polymer dynamic properties) can be postulated as a reason for the MW-independent effective viscosity of PS in 7 nm $SiO_2$ NP packings. The infiltration dynamics is controlled by the increased viscous resistance coming from the slip length term. If this term is large enough to overpower changes in the intrinsic viscosity with increasing MW, it is possible that the infiltration dynamics exhibit MW independence and thus MW-independent confined viscosity.[63]

Prior studies have reported slippage of wetting fluids on solid surfaces.[64] Considering the favorable interactions between the polymer and the NP (the contact angle of PS on $SiO_2$ is 20°), however, it seems unlikely for the polymer to slip on the NP surface. Additionally, the chains adsorbed on the solid walls may entangle with the flowing chains, leading to strong suppression of slip. At high shear velocities of the order of micrometers per second, the adsorbed chains can disentangle from the flowing chains, leading to revival of slip.[65,66] As mentioned earlier, however, the shear rate in the CaRI process is not high enough to lead to any significant shear-induced disentangling between surface-adsorbed and bulk chains, which means that slip is not significant in describing the flow dynamics.

While the reptation-driven plug-flow mechanism can explain the enhanced mobility of confined polymers in 27 nm $SiO_2$ packings and accounts for the linear scaling of confined viscosity with MW, the model cannot explain the constant effective viscosity of confined PS in the packings of 7 nm $SiO_2$ particles. One possible reason is that the model was developed to consider a linear flow regime in which polymers obey Gaussian chain statistics.[58,67] This model would not be accurate under a high capillary pressure generated in such narrow pores where the chain conformation may be substantially perturbed. A theoretical framework for MW-independent viscosity has been proposed for polymer melts flowing under high pressures.[58] The model states that polymers flowing under high capillary pressure experience increased stretching due to incomplete screening of the excluded volume. This stretching leads to transitioning from the linear flow regime to a nonlinear flow regime at a crossover pressure gradient, which depends on the chain size and the pore radius. The reptation model applied to such a nonideal flow case is shown to behave independently of the MW of the polymer (see the Supporting Information for details). The high capillary pressures in 7 nm $SiO_2$ NP packings are indeed above such a crossover pressure gradient.

The average pore size in the 7 nm $SiO_2$ packings is 2 nm, which is comparable to the Kuhn segment length of the polymer. Such a state of extreme nanoconfinement is referred to as the hyperconfined condition.[31,67] Polymer chains experience excluded volume interactions due to incomplete shielding under hyperconfinement, which leads to extreme axial stretching of the chains.[31,67] To avoid the entropic penalty of stretching, the chains segregate to occupy different regions, forming a train of chains occupying pores. Such hyperconfinement occurs above a critical chain size (or MW of the polymer) relative to the pore size, and this threshold for the 7 nm $SiO_2$ packings is at a lower MW than for the 27 nm $SiO_2$ NP packings (see the Supporting Information for detailed calculations). The ranges of MW of polymers confined in the 7 nm $SiO_2$ packings are all in the hyperconfined regime. Although we do not fully understand the exact correlation between hyperconfinement and the observed flow behavior, we point out that the level of confinement that leads to the chain size-independent viscosity coincides with the onset of hyperconfinement.

**Segmental Slowdown.** Segmental slowdown has been reported previously near attractive surfaces due to the adsorption of chain segments and/or nonbulk-like conformation of the polymer chains under confinement. In addition, segmental slowdown has been reported near impenetrable surfaces and highly confined spaces due to reduced free volume available for polymer motion. In the CaRI system, there is significant confinement of the polymers in the pores of NPs along with a large interfacial area between the polymer and the NPs. In a previous study on PS confined in the interstices of $SiO_2$ NP packings, a dramatic increase in $T_g$ was observed with increasing confinement (decreasing NP radius) and the effects were mostly understood as originating from the loss of conformational entropy due to geometric confinement of the polymer.[32] Studies on undersaturated CaRI films


https://doi.org/10.1021/acs.macromol.2c00145
Macromolecules 2022, 55, 4492−4501

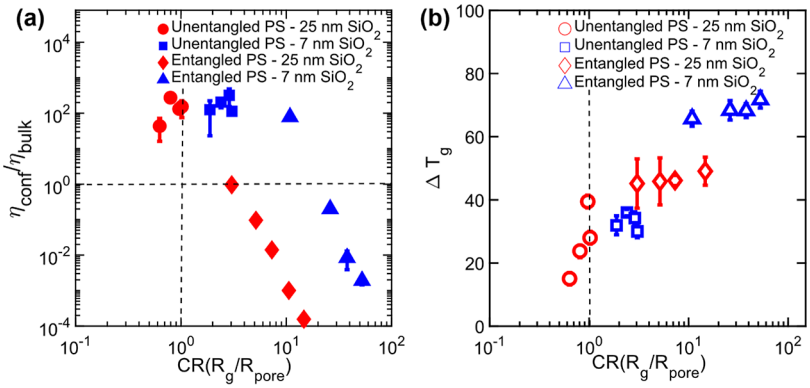


**Figure 6.** (a) Confined viscosity measured for PS (8k g/mol to 4M g/mol) infiltrating $SiO_2$ NP packings at different CRs—unentangled PS (8k g/mol to 21k g/mol) in $SiO_2$ of 7−77 nm diameter measured at 130 °C, shown in circles and squares; entangled PS (173k g/mol to 4M g/mol) in $SiO_2$ of 27 nm measured at 165 °C, shown in diamonds; and entangled PS(173k g/mol to 4M g/mol) in $SiO_2$ of 7 nm measured at 165 °C, shown in triangles. (b) Difference between the glass transition temperature in confinement over the bulk ($\Delta T_g$) at various CRs for the three scenarios in (a). Adapted with permission from Hor, J. L.; Wang, H.; Fakhraai, Z.; Lee, D. Effect of Physical Nanoconfinement on the Viscosity of Unentangled Polymers during Capillary Rise Infiltration. *Macromolecules* **2018,** *51 (14),* 5069−5078. https://doi.org/10.1021/acs.macromol.8b00966. Copyright 2018 American Chemical Society.

showed that the polymer exists in the highly confined regions of the packings between the particles, leading to high $T_g$.[3,32] Thus, the source of increase in $T_g$ of entangled polymer chains in the 7 and 27 nm $SiO_2$ NP packings comes mainly from the high geometrical confinement experienced by the polymer chain in the nanopores. The unique nature of the concave pores also plays a role by decreasing the free volume and increasing the packing density, which is strikingly different from PS trapped in convex pores like those in AAO. The pores of the NP packing, where the concave nature of the pores can be hindering segmental relaxation, lead to an increase in $T_g$.[68] An additional increase in slowdown of entangled polymers in 7 nm packings over 27 nm packings comes from not only increase in confinement but also increase in the interfacial area between the polymer and $SiO_2$ NP. As shown in Figure 4, in the CR range of 10−15, the increase in $T_g$ for PS-4M in 27 nm $SiO_2$ NP packings is 50 K, whereas PS-173k in 7 nm $SiO_2$ NP, despite being at the same level of confinement (same CR), shows an increase of 65 K in $T_g$, which indicates that the interfacial area also contributes to the segmental slowdown of polymers in CaRI films.

To check whether an increase in the interfacial area alone can explain the trends in $T_g$, we plot the increase in $T_g$ for unentangled and entangled PS in $SiO_2$ as a function of the interfacial area/volume of the NP packings (see the Supporting Information for details). While the large interfacial area is an important factor contributing to the large increase that we observe, it cannot completely account for the trends alone. A combination of increasing confinement and interfacial area between the polymer−NP can explain the observed $T_g$ trends. As the polymer size is increased (and/or NP size is reduced), the polymer chains experience larger confinement and an increase in the interfacial area between the polymer and NP, leading to the observed increase in $T_g$.

**Decoupling of Translational and Segmental Mobility.** Unlike earlier reports of PS chains in the pores of AAO membranes which showed enhanced translational mobility and either little change or an increase in the segmental dynamics,[26,27] the increase in translational motion of confined polymers in $SiO_2$ NP packings accompanies a drastic reduction in segmental mobility; that is, changes in the segmental dynamics do not translate to corresponding changes in the infiltration dynamics. Our results demonstrate that extreme nanoconfinement of polymers can decouple dynamics occurring over different length scales over different timescales. The time−temperature superposition relationship connecting the viscosity and $T_g$ has been shown to fail in some nanoconfined systems.[69,70] One notable study, for example, has shown that both the $T_g$ and the diffusivity of poly(isobutyl methacrylate) confined between two weakly interacting surfaces increase.[69] An increase in the diffusivity of confined chains was attributed to the reduction in the friction coefficient caused by the weakly interacting interface, whereas the slowdown of segmental relaxation was thought to be affected by confinement.

The conflicting effects of confinement on chain and segmental motion in this work arise from the disparate effects acting independently on different length scales. With increasing confinement, entangled chains participate in a reptation-driven flow into nanopores, which leads to faster-than-bulk translational motion. On the other hand, confining polymers in nanoscopic pores with concave curvature and increasing the particle−polymer interface slows down segmental dynamics of the confined polymers in the nanopores. Thus, the effects of confinement can be quite different at different length scales for entangled polymers confined in NP packings. In the next section, we summarize our results on unentangled and entangled polymers to provide a picture of the effect of confinement on the motion of polymers at the chain and segmental levels in CaRI packings.

**Summary of the Confinement Effect on the Translational and Segmental Dynamics of Unentangled and Entangled Polymers in NP Packings.** By combining data on $T_g$ and effective viscosity obtained from the CaRI of unentangled polymers from our prior work[25] with the data on entangled polymers from this study, we summarize the effect of nanoconfinement on the segmental and translational motion of confined polymers over a wide range of CRs and MWs. Figure 6a shows normalized viscosity of both unentangled[25] and entangled polymers in $SiO_2$ NP packings. While the viscosity of unentangled polymers increases with increasing confinement, the effective viscosity decreases with increasing confinement in CaRI of entangled polymers in 27 nm packings. This can be understood by considering the role of the two terms in


https://doi.org/10.1021/acs.macromol.2c00145
Macromolecules 2022, 55, 4492−4501

eq 4. The first term is effective for underconfined polymers ($R_{pore} > R_g$), while the second term controls the motion of confined polymers ($R_{pore} < R_g$). In the first term, $R_{eff}$ decreases with increasing confinement, which explains the increasing viscosity upon confinement for unentangled polymers whose CR < 1. The second term, which is effective for confined entangled polymers (CR > 1), increases with decreasing pore size, leading to an effective reduction in viscosity. The motion of entangled polymers occurs by reptation in a mesh of constraints under the action of capillary pressure—this motion is faster than their bulk counterparts. Unentangled polymers are slowed down by the reduction in the pore radius due to the adsorption of polymers on the pore surface. The microscopic flow model developed in ref 53 qualitatively explains trends in our confined viscosity qualitatively over a wide range of confinement (CR from 1 to 10). The confinement-independent viscosity of PS in 7 nm $SiO_2$ packings, however, requires further consideration and theoretical development.

Figure 6b shows $T_g$s obtained for unentangled and entangled polymers with increasing confinement. We see that with increasing confinement (smaller pores or larger polymer), the segmental dynamics are further slowed down. This can be understood by the combined effect of geometric confinement and the dynamical slowdown of the interfacial layer. In the weakly confined regime (CR < 1), the $\Delta T_g$ increases with increasing CR due to increasing confinement. When the chain size becomes larger than the pore size, a further increase in $\Delta T_g$ is observed. The role of confinement is even more evident in the larger $T_g$ increase in 7 nm $SiO_2$ packings (as compared to the 27 nm packings), where due to the larger geometric confinement and an increase in interfacial area, the $T_g$ increases by 65 K over bulk.

The dependence of translational and segmental dynamics on the CR in Figure 6 shows that one universal parameter such as the CR cannot describe the entire trend (data does not collapse with pore size/chain size as seen in previous studies[53,71]). The effect of nanoconfinement on polymer dynamics arises from a complex interplay of chain entanglement, extent of confinement, the pore curvature, and the absolute size of confining pores. The extent of confinement as defined by the CR influences the deviations from bulk dynamics both at the chain and segmental levels. The radius of the pore is another key parameter; we observe that when $R_{pore}$ approaches the Kuhn length of the polymer, the chain viscosity becomes independent of MW—an observation that cannot be fully explained by the existing models of polymer dynamics.

## CONCLUSIONS

Chain and segmental dynamics of entangled PS infiltration by CaRI into $SiO_2$ NP packings are studied using ellipsometry to probe the effect of nanoconfinement on polymer mobility. In the range of CRs probed (CR from 3 to 55), increasing confinement has opposite effects on the polymer dynamics at the chain and segmental levels. Capillary rise dynamics of entangled PS in 27 nm $SiO_2$ NP packing show that the confined viscosity is reduced when compared to the bulk viscosity. Contrary to enhancement in translational mobility, confinement reduces the segmental motion across all levels of confinement with the effect increasing with decreasing particle size owing to an increase in confinement along with a greater interface between the polymer and the attractive $SiO_2$ NP. We also report a MW-independent value of effective viscosity in the 7 nm $SiO_2$ NP packings. The trends in the confined viscosity are explained qualitatively by theoretical arguments of a dead zone of adsorbed polymers slowing down chain motion for underconfined polymers, whereas reptation-like plug flow leading to enhanced microscopic flow of entangled chains. Although we do not fully understand the origin of the MW-independent effective viscosity of polymers in 7 nm $SiO_2$ NP packings, nonlinear polymer flow or hyperconfinement effects may play a role. Reduced segmental mobility is understood to be an effect of high confinement of polymer chains in the concave pores of the NP packing and the large interfacial area between $SiO_2$ and polymer under confinement. Thus, the effect of confinement on motion of polymers is different at different length scales and depends on the relative role of the macroscopic and microscopic mechanisms of motion.

In this work, only the size of silica NPs and the MW of the polymer are varied, thus keeping the interfacial energy between the polymer and the NP constant. In a recent work, a technique to modify the interfacial energy between PS and $SiO_2$ NPs by coating ultrathin metal oxides such as $WO_3$ and $TiO_2$ using atomic layer deposition has been reported.[72] This approach can be used to investigate the effect of interfacial energy on the translational and segmental motion of highly confined polymers in NP packings. The enhanced translational motion of high-MW polymers can be used to facilitate their infiltration into NP packings to fabricate highly loaded nanocomposite membranes and films. Moreover, such enhanced motion of polymers in nanopores is advantageous for performing reactions to enable upcycling of polymers *via* heterogenous catalysis, which typically require intimate contact between nanoporous catalysts and polymers. Increasing $T_g$ also could be advantageous for applications that require high temperatures, enabling wider operating conditions for composite materials prepared *via* CaRI.

## ASSOCIATED CONTENT

### Supporting Information

The Supporting Information is available free of charge at https://pubs.acs.org/doi/10.1021/acs.macromol.2c00145.

Bulk viscosity, contact angle, and surface tension calculations; $T_g$ extraction from the ellipsometric data; constant viscosity with MW in 7 nm silica NP packings; role of interfacial area of PS−silica in increase of $T_g$; viscosity data plotted against $1/r$; shear rate calculations; scaling of viscosity at a fixed distance from $T_g$; and contact angle sensitivity analysis (PDF)

## AUTHOR INFORMATION


### Corresponding Author

**Daeyeon Lee** − *Department of Chemical and Biomolecular Engineering, University of Pennsylvania, Philadelphia, Pennsylvania 19104, United States;* orcid.org/0000-0001-6679-290X; Email: daeyeon@seas.upenn.edu

### Author

**R. Bharath Venkatesh** − *Department of Chemical and Biomolecular Engineering, University of Pennsylvania, Philadelphia, Pennsylvania 19104, United States*

Complete contact information is available at: https://pubs.acs.org/10.1021/acs.macromol.2c00145




https://doi.org/10.1021/acs.macromol.2c00145
Macromolecules 2022, 55, 4492−4501

### Author Contributions

The manuscript was written through contributions of all authors. All authors have given approval to the final version of the manuscript.

### Notes

The authors declare no competing financial interest.

## ■ ACKNOWLEDGMENTS

We thank Prof. Zahra Fakhraai, Dr. Haonan Wang, and Yueli Chen for their help with the ellipsometry measurements. This work was supported by Penn MRSEC (DMR 1720530). This work was carried out in part at the Singh Center for Nanotechnology, which is supported by the NSF National Nanotechnology Coordinated Infrastructure Program under grant NNCI-2025608.

## ■ ABBREVIATIONS

CaRI:capillary rise infiltration; NP:nanoparticle; $SiO_2$:silica; PS:polystyrene; $T_g$:glass transition temperature; CR:confinement ratio

## ■ REFERENCES

(1) Cauda, V.; Stassi, S.; Bejtka, K.; Canavese, G. Nanoconfinement: An Effective Way to Enhance PVDF Piezoelectric Properties. *ACS Appl. Mater. Interfaces* **2013**, *5*, 6430−6437.

(2) Huang, Y.-R.; Jiang, Y.; Hor, J. L.; Gupta, R.; Zhang, L.; Stebe, K. J.; Feng, G.; Turner, K. T.; Lee, D. Polymer Nanocomposite Films with Extremely High Nanoparticle Loadings via Capillary Rise Infiltration (CaRI). *Nanoscale* **2015**, *7*, 798−805.

(3) Hor, J. L.; Jiang, Y.; Ring, D. J.; Riggleman, R. A.; Turner, K. T.; Lee, D. Nanoporous Polymer-Infiltrated Nanoparticle Films with Uniform or Graded Porosity via Undersaturated Capillary Rise Infiltration. *ACS Nano* **2017**, *11*, 3229−3236.

(4) Magrini, T.; Bouville, F.; Lauria, A.; Le Ferrand, H.; Niebel, T. P.; Studart, A. R. Transparent and Tough Bulk Composites Inspired by Nacre. *Nat. Commun.* **2019**, *10*, 2794.

(5) Qiang, Y.; Turner, K. T.; Lee, D. Polymer-Infiltrated Nanoplatelet Films with Nacre-like Structure: Via Flow Coating and Capillary Rise Infiltration (CaRI). *Nanoscale* **2021**, *13*, 5545−5556.

(6) De Jongh, P. E.; Eggenhuisen, T. M. Melt Infiltration: An Emerging Technique for the Preparation of Novel Functional Nanostructured Materials. *Adv. Mater.* **2013**, *25*, 6672−6690.

(7) Venkatesh, R. B.; Han, S. H.; Lee, D. Patterning Polymer-Filled Nanoparticle Films via Leaching-Enabled Capillary Rise Infiltration (LeCaRI). *Nanoscale Horizons* **2019**, *4*, 933−939.

(8) Manohar, N.; Stebe, K. J.; Lee, D. Solvent-Driven Infiltration of Polymer (SIP) into Nanoparticle Packings. *ACS Macro Lett.* **2017**, *6*, 1104−1108.

(9) Wang, C.; Isaacson, S. G.; Wang, Y.; Lionti, K.; Volksen, W.; Magbitang, T. P.; Chowdhury, M.; Priestley, R. D.; Dubois, G.; Dauskardt, R. H. Surface Chemical Functionalization to Achieve Extreme Levels of Molecular Confinement in Hybrid Nanocomposites. *Adv. Funct. Mater.* **2019**, *29*, 1903132.

(10) Qiang, Y.; Manohar, N.; Stebe, K. J.; Lee, D. Polymer Blend-Filled Nanoparticle Films: Via Monomer-Driven Infiltration of Polymer and Photopolymerization. *Mol. Syst. Des. Eng.* **2018**, *3*, 96−102.

(11) Martín, J.; Nogales, A.; Martín-González, M. The Smectic−Isotropic Transition of P3HT Determines the Formation of Nanowires or Nanotubes into Porous Templates. *Macromolecules* **2013**, *46*, 1477−1483.

(12) Martín, J.; Martín-González, M. The Use of PEEK Nanorod Arrays for the Fabrication of Nanoporous Surfaces under High Temperature: SiNx Example. *Nanoscale* **2012**, *4*, 5608−5613.

(13) Wu, H.; Higaki, Y.; Takahara, A. Molecular Self-Assembly of One-Dimensional Polymer Nanostructures in Nanopores of Anodic Alumina Oxide Templates. *Prog. Polym. Sci.* **2018**, *77*, 95−117.

(14) Tsai, C.-C.; Chen, J.-T. Effect of the Polymer Concentration on the Rayleigh-Instability-Type Transformation in Polymer Thin Films Coated in the Nanopores of Anodic Aluminum Oxide Templates. *Langmuir* **2015**, *31*, 2569−2575.

(15) Chen, J.-T.; Zhang, M.; Russell, T. P. Instabilities in Nanoporous Media. *Nano Lett.* **2007**, *7*, 183−187.

(16) Kim, J.; Cho, Y.; Kim, S.; Lee, J. 3D Cocontinuous Composites of Hydrophilic and Hydrophobic Soft Materials: High Modulus and Fast Actuation Time. *ACS Macro Lett.* **2017**, *6*, 1119−1123.

(17) Jiang, Y.; Hor, J. L.; Lee, D.; Turner, K. T. Toughening Nanoparticle Films via Polymer Infiltration and Confinement. *ACS Appl. Mater. Interfaces* **2018**, *10*, 44011−44017.

(18) Venkatesh, R. B.; Manohar, N.; Qiang, Y.; Wang, H.; Tran, H. H.; Kim, B. Q.; Neuman, A.; Ren, T.; Fakhraai, Z.; Riggleman, R. A.; Stebe, K. J.; Turner, K.; Lee, D. Polymer-Infiltrated Nanoparticle Films Using Capillarity-Based Techniques: Toward Multifunctional Coatings and Membranes. *Annu. Rev. Chem. Biomol. Eng.* **2021**, *12*, 411−437.

(19) Tran, H. H.; Venkatesh, R. B.; Kim, Y.; Lee, D.; Riassetto, D. Multifunctional Composite Films with Vertically Aligned ZnO Nanowires by Leaching-Enabled Capillary Rise Infiltration. *Nanoscale* **2019**, *11*, 22099−22107.

(20) Tran, H. H.; Kim, Y.; Ternon, C.; Langlet, M.; Riassetto, D.; Lee, D. Lubricant Depletion-Resistant Slippery Liquid-Infused Porous Surfaces via Capillary Rise Lubrication of Nanowire Array. *Adv. Mater. Interfaces* **2021**, *8*, 2002058.

(21) Wang, H.; Qiang, Y.; Shamsabadi, A. A.; Mazumder, P.; Turner, K. T.; Lee, D.; Fakhraai, Z. Thermal Degradation of Polystyrene under Extreme Nanoconfinement. *ACS Macro Lett.* **2019**, *8*, 1413−1418.

(22) Kim, B. Q.; Qiang, Y.; Turner, K. T.; Choi, S. Q.; Lee, D. Heterostructured Polymer-Infiltrated Nanoparticle Films with Cavities via Capillary Rise Infiltration. *Adv. Mater. Interfaces* **2021**, *8*, 2001421.

(23) Tennakoon, A.; Wu, X.; Paterson, A. L.; Patnaik, S.; Pei, Y.; LaPointe, A. M.; Ammal, S. C.; Hackler, R. A.; Heyden, A.; Slowing, I. I.; Coates, G. W.; Delferro, M.; Peters, B.; Huang, W.; Sadow, A. D.; Perras, F. A. Catalytic Upcycling of High-Density Polyethylene via a Processive Mechanism. *Nat. Catal.* **2020**, *3*, 893−901.

(24) Hor, J. L.; Wang, H.; Fakhraai, Z.; Lee, D. Effects of Polymer-Nanoparticle Interactions on the Viscosity of Unentangled Polymers under Extreme Nanoconfinement during Capillary Rise Infiltration. *Soft Matter* **2018**, *14*, 2438−2446.

(25) Hor, J. L.; Wang, H.; Fakhraai, Z.; Lee, D. Effect of Physical Nanoconfinement on the Viscosity of Unentangled Polymers during Capillary Rise Infiltration. *Macromolecules* **2018**, *51*, 5069−5078.

(26) Yao, Y.; Alexandris, S.; Henrich, F.; Auernhammer, G.; Steinhart, M.; Butt, H.-J.; Floudas, G. Complex Dynamics of Capillary Imbibition of Poly(Ethylene Oxide) Melts in Nanoporous Alumina. *J. Chem. Phys.* **2017**, *146*, 203320.

(27) Shin, K.; Obukhov, S.; Chen, J.-T.; Huh, J.; Hwang, Y.; Mok, S.; Dobriyal, P.; Thiyagarajan, P.; Russell, T. P. Enhanced Mobility of Confined Polymers. *Nat. Mater.* **2007**, *6*, 961−965.

(28) Cencha, L. G.; Urteaga, R.; Berli, C. L. A. Interferometric Technique To Determine the Dynamics of Polymeric Fluids under Strong Confinement. *Macromolecules* **2018**, *51*, 8721−8728.

(29) Tung, W.-S.; Composto, R. J.; Riggleman, R. A.; Winey, K. I. Local Polymer Dynamics and Diffusion in Cylindrical Nanoconfinement. *Macromolecules* **2015**, *48*, 2324−2332.

(30) Sussman, D. M.; Tung, W.-S.; Winey, K. I.; Schweizer, K. S.; Riggleman, R. A. Entanglement Reduction and Anisotropic Chain and Primitive Path Conformations in Polymer Melts under Thin Film and Cylindrical Confinement. *Macromolecules* **2014**, *47*, 6462−6472.

(31) Pressly, J. F.; Riggleman, R. A.; Winey, K. I. Polymer Diffusion Is Fastest at Intermediate Levels of Cylindrical Confinement. *Macromolecules* **2018**, *51*, 9789−9797.



https://doi.org/10.1021/acs.macromol.2c00145
*Macromolecules* 2022, 55, 4492−4501

(32) Wang, H.; Hor, J. L.; Zhang, Y.; Liu, T.; Lee, D.; Fakhraai, Z. Dramatic Increase in Polymer Glass Transition Temperature under Extreme Nanoconfinement in Weakly Interacting Nanoparticle Films. *ACS Nano* **2018**, *12*, 5580−5587.
(33) Vogel, H. The Temperature Dependent Viscosity Law for Liquids. *Phys. Z.* **1921**, *22*, 645−646.
(34) Fulcher, G. S. Analysis of Recent Measurements of the Viscosity of Glasses. *J. Am. Ceram. Soc.* **1925**, *8*, 339−355.
(35) Tammann, G.; Hesse, W. Die Abhängigkeit der Viscosität von der Temperatur bie unterkühlten Flüssigkeiten. *Zeitschrift für Anorg. und Allg. Chemie* **1926**, *156*, 245−257.
(36) Washburn, E. W. The Dynamics of Capillary Flow. *Phys. Rev.* **1921**, *17*, 273−283.
(37) Zhmud, B. V.; Tiberg, F.; Hallstensson, K. Dynamics of Capillary Rise. *J. Colloid Interface Sci.* **2000**, *228*, 263−269.
(38) Siebold, A.; Walliser, A.; Nardin, M.; Oppliger, M.; Schultz, J. Capillary Rise for Thermodynamic Characterization of Solid Particle Surface. *J. Colloid Interface Sci.* **1997**, *186*, 60−70.
(39) Reyssat, M.; Sangne, L. Y.; Van Nierop, E. A.; Stone, H. A. Imbibition in Layered Systems of Packed Beads. *EPL* **2009**, *86*, 56002.
(40) Leoni, F.; Kierlik, E.; Rosinberg, M. L.; Tarjus, G. Spontaneous Imbibition in Disordered Porous Solids: A Theoretical Study of Helium in Silica Aerogels. *Langmuir* **2011**, *27*, 8160−8170.
(41) Gruener, S.; Huber, P. Capillarity-Driven Oil Flow in Nanopores: Darcy Scale Analysis of Lucas−Washburn Imbibition Dynamics. *Transp. Porous Media* **2019**, *126*, 599−614.
(42) Kiepsch, S.; Pelster, R. Interplay of Vapor Adsorption and Liquid Imbibition in Nanoporous Vycor Glass. *Phys. Rev. E* **2016**, *93*, 1−11.
(43) Tsunazawa, Y.; Yokoyama, T.; Nishiyama, N. An Experimental Study on the Rate and Mechanism of Capillary Rise in Sandstone. *Prog. Earth Planet. Sci.* **2016**, *3*, 1−10.
(44) Alava, M.; Dubé, M.; Rost, M. Imbibition in Disordered Media. *Adv. Phys.* **2004**, *53*, 83−175.
(45) Gruener, S.; Huber, P. Imbibition in Mesoporous Silica: Rheological Concepts and Experiments on Water and a Liquid Crystal. *J. Phys. Condens. Matter* **2011**, *23*, 184109.
(46) Cai, J.; Jin, T.; Kou, J.; Zou, S.; Xiao, J.; Meng, Q. Lucas-Washburn Equation-Based Modeling of Capillary-Driven Flow in Porous Systems. *Langmuir* **2021**, *37*, 1623−1636.
(47) Rémond, S.; Gallias, J. L.; Mizrahi, A. Characterization of Voids in Spherical Particle Systems by Delaunay Empty Spheres. *Granul. Matter* **2008**, *10*, 329−334.
(48) Bertei, A.; Nucci, B.; Nicolella, C. Effective Transport Properties in Random Packings of Spheres and Agglomerates. *Chem. Eng. Trans.* **2013**, *32*, 1531−1536.
(49) Seemann, R.; Jacobs, K.; Blossey, R. Polystyrene Nanodroplets. *J. Phys. Condens. Matter* **2001**, *13*, 4915−4923.
(50) Fox, T. G.; Flory, P. J. Viscosity—Molecular Weight and Viscosity—Temperature Relationships for Polystyrene and Polyisobutylene. *J. Am. Chem. Soc.* **1948**, *70*, 2384−2395.
(51) Fox, T. G.; Flory, P. J. Second-Order Transition Temperatures and Related Properties of Polystyrene. I. Influence of Molecular Weight. *J. Appl. Phys.* **1950**, *21*, 581−591.
(52) Fox, T. G.; Flory, P. J. The Glass Temperature and Related Properties of Polystyrene. Influence of Molecular Weight. *J. Polym. Sci.* **1954**, *14*, 315−319.
(53) Yao, Y.; Butt, H.-J.; Floudas, G.; Zhou, J.; Doi, M. Theory on Capillary Filling of Polymer Melts in Nanopores. *Macromol. Rapid Commun.* **2018**, *39*, 1800087.
(54) Dimitrov, D. I.; Milchev, A.; Binder, K. Capillary Rise in Nanopores: Molecular Dynamics Evidence for the Lucas-Washburn Equation. *Phys. Rev. Lett.* **2007**, *99*, 054501.
(55) Shavit, A.; Riggleman, R. A. The Dynamics of Unentangled Polymers during Capillary Rise Infiltration into a Nanoparticle Packing. *Soft Matter* **2015**, *11*, 8285−8295.
(56) Digilov, R. M. Capillary Rise of a Non-Newtonian Power Law Liquid: Impact of the Fluid Rheology and Dynamic Contact Angle. *Langmuir* **2008**, *24*, 13663−13667.
(57) Cao, B.-Y.; Yang, M.; Hu, G.-J. Capillary Filling Dynamics of Polymer Melts in Nanopores: Experiments and Rheological Modelling. *RSC Adv.* **2016**, *6*, 7553−7559.
(58) Johner, A.; Shin, K.; Obukhov, S. Nanofluidity of a Polymer Melt: Breakdown of Poiseuille's Flow Model. *EPL* **2010**, *91*, 38002.
(59) Muthukumar, M. Entropic Barrier Model for Polymer Diffusion in Concentrated Polymer Solutions and Random Media. *J. Non. Cryst. Solids* **1991**, *131*−*133*, 654−666.
(60) Jiang, N.; Shang, J.; Di, X.; Endoh, M. K.; Koga, T. Formation Mechanism of High-Density, Flattened Polymer Nanolayers Adsorbed on Planar Solids. *Macromolecules* **2014**, *47*, 2682−2689.
(61) Tu, C.-H.; Zhou, J.; Doi, M.; Butt, H.-J.; Floudas, G. Interfacial Interactions during in Situ Polymer Imbibition in Nanopores. *Phys. Rev. Lett.* **2020**, *125*, 127802.
(62) Tu, C.-H.; Zhou, J.; Butt, H.-J.; Floudas, G. Adsorption Kinetics of Cis-1,4-Polyisoprene in Nanopores by in Situ Nanodielectric Spectroscopy. *Macromolecules* **2021**, *54*, 6267−6274.
(63) Chen, F.; Peng, D.; Lam, C.-H.; Tsui, O. K. C. Viscosity and Surface-Promoted Slippage of Thin Polymer Films Supported by a Solid Substrate. *Macromolecules* **2015**, *48*, 5034−5039.
(64) Neto, C.; Evans, D. R.; Bonaccurso, E.; Butt, H.-J.; Craig, V. S. J. Boundary Slip in Newtonian Liquids: A Review of Experimental Studies. *Reports Prog. Phys.* **2005**, *68*, 2859−2897.
(65) Mhetar, V.; Archer, L. A. Slip in Entangled Polymer Melts. 2. Effect of Surface Treatment. *Macromolecules* **1998**, *31*, 8617−8622.
(66) Léger, L.; Hervet, H.; Massey, G.; Durliat, E. Wall Slip in Polymer Melts. *J. Phys. Condens. Matter* **1997**, *9*, 7719−7740.
(67) Lee, N.-K.; Farago, J.; Meyer, H.; Wittmer, J. P.; Baschnagel, J.; Obukhov, S. P.; Johner, A. Non-Ideality of Polymer Melts Confined to Nanotubes. *EPL* **2011**, *93*, 48002.
(68) Wang, H.; Kearns, K. L.; Zhang, A.; Arabi Shamsabadi, A.; Jin, Y.; Bond, A.; Hurney, S. M.; Morillo, C.; Fakhraai, Z. Effect of Nanopore Geometry in the Conformation and Vibrational Dynamics of a Highly Confined Molecular Glass. *Nano Lett.* **2021**, *21*, 1778−1784.
(69) Geng, K.; Katsumata, R.; Yu, X.; Ha, H.; Dulaney, A. R.; Ellison, C. J.; Tsui, O. K. C. Conflicting Confinement Effects on the Tg, Diffusivity, and Effective Viscosity of Polymer Films: A Case Study with Poly(Isobutyl Methacrylate) on Silica and Possible Resolution. *Macromolecules* **2017**, *50*, 609−617.
(70) Hao, Z.; Ghanekarade, A.; Zhu, N.; Randazzo, K.; Kawaguchi, D.; Tanaka, K.; Wang, X.; Simmons, D. S.; Priestley, R. D.; Zuo, B. Mobility Gradients Yield Rubbery Surfaces on Top of Polymer Glasses. *Nature* **2021**, *596*, 372−376.
(71) Choi, J.; Hore, M. J. A.; Meth, J. S.; Clarke, N.; Winey, K. I.; Composto, R. J. Universal Scaling of Polymer Diffusion in Nanocomposites. *ACS Macro Lett.* **2013**, *2*, 485−490.
(72) Ren, T.; Huang, R.; Gorte, R. J.; Lee, D. Modulating Interactions between Molten Polystyrene and Porous Solids Using Atomic Layer Deposition. *Langmuir* **2021**, *37*, 14520−14526.


https://doi.org/10.1021/acs.macromol.2c00145
*Macromolecules* 2022, 55, 4492−4501